# First-principles simulation of the electronic stopping power of He ions in Al at finite temperature

Su-Na Pang,[1] Feng Wang,[1,*] Ya-Ting Sun,[1] Fei Mao,[2,†] and Xiao-Li Wang[3]
[1]*School of Physics, Beijing Institute of Technology, Beijing 100081, China*
[2]*School of Nuclear Science and Technology, University of South China, Hengyang 421001, China*
[3]*School of Mechanical Engineering, Beijing Institute of Technology, Beijing 100081, China*

(Received 10 September 2021; accepted 22 February 2022; published 10 March 2022)

The electronic stopping power of low-energy He projectile particles moving through an Al film under channeling and off-channeling trajectories and its temperature dependence are studied by combining the time-dependent density-functional-theory method with molecular dynamics simulations. The results show that the effect of target temperature on target stopping power can be divided into two aspects which are derived from the target electron and target ion. Below 500 K, the effect of the target-electron temperature on target stopping power is almost negligible. The influence of the target-ion temperature on target stopping power can be divided into two aspects which are derived from the displacement and energy dissipation of target ions. The displacement of the target ion can result in two trends that change the target stopping power: (1) The target ion is closer to the center of lattice channel after displacement, which leads to the increase of target stopping power. (2) The target ion is farther away from the center of the lattice channel after displacement, which leads to the decrease in target stopping power. As the temperature increases, the target ions are more likely to appear farther away from the lattice channel than closer to the center of the lattice channel, so the average displacement of the target ions will lead to a decreasing trend of the target stopping power with the increase of temperature. Under the condition of a given ionic density in the target, the energy dissipation capacity of target ions increases with the increase of temperature, resulting in the tendency of the target stopping power to increase with the increase of temperature. Our calculated stopping powers are in good agreement with the experimental data and reproduced the deviation from velocity proportionality found in the experimental results for a $He^+$ ion in Al, validating our approach and numerical implementation.

DOI: 10.1103/PhysRevA.105.032803

## I. INTRODUCTION

Nuclear batteries convert radiation directly into electric energy by utilizing the energy released either from nuclear fission or through radioactive decay. Nuclear batteries, characterized by their small size, light weight, stronger durability in harsh conditions, and higher volumetric energy density (thus longer battery life), may be used for the next generation of satellites, spacecraft, and space probes [1–3]. Implantable medical devices such as pacemakers have also utilized the unique characteristics of nuclear batteries. In addition, nuclear batteries are widely used in microelectric machinery, electronic products such as mobile phones, and electric vehicles [4,5]. Therefore, the vigorous development of nuclear batteries has a significant impact on practical applications.

On the other hand, ion irradiation is a common method to modify and analyze the surface structure of materials. The interaction of ions with atoms of target materials was extensively studied in the early days of atomic physics [6,7]. Electronic stopping power $S_e$ is an important quantity to predict and understand the influence of particle radiation in matter. $S_e$ can explain the electronic excitation that occurs through the Coulomb interaction with the ion. $S_e$ can be represented by $dE/dx$, that is, the energy lost per unit length of the projectile ion in the path as the projectile moves through the material.

$S_e$ of materials exposed to high-intensity and ultrashort laser pulses have been attracting substantial interest from both fundamental and technological points of view. Ultrashort laser pulses can instantaneously control a material's electronic states [8–17], such as electron temperature, without destroying its configuration. Electronic temperature has a sensitive effect on the $S_e$, so ultrashort laser pulses can provide a new degree of freedom to regulate $S_e$ without changing the material configuration. We are very interested in $S_e$ at finite temperatures. To the best of our knowledge, a time-domain electron dynamics simulation based on the time-dependent density-functional theory (TDDFT) is currently one of the most reliable theoretical approaches to analyze the nonequilibrium response of materials under ion irradiation and to calculate the nonadiabatic energy transfer between ions and electrons [18,19]. Note that temperature should remain one of the most important variables acting on stopping power of the material, participating in the mechanisms of electronic stopping and nuclear stopping. This is relevant because temperature can modify the stopping power of the material, which is actually a consequence of the change in the respective electronic and nuclear structures. Despite its fundamental role,

*wangfeng01@tsinghua.org.cn
†maofei@mail.bnu.edu.cn

 

this variable is ignored in most of the theoretical approaches employed to characterize the stopping of materials. Particularly, the TDDFT model assumes that the initial temperature of the target material is zero, so that the stopping properties at finite temperature remain neglected within this approach. The effect of finite electron temperature on $S_e$ is one of the topics of this article.

Furthermore, the electronic excitation strongly depends on the projectile charge and velocity. The study of energy transfer between slow ions (speeds less than Bohr's velocity) and targets plays a very important role in materials science [20]. For low projectiles, $S_e$ of metals is predicted to be proportional to the velocity [21–23]. However, what is most interesting to us is that an unusual phenomenon, a deviation from the velocity-proportional stopping power, was discovered for a $He^+$ ion traversing through Al in experiment [24]. Obviously, by considering the dynamics of electrons and ions in real-time simulations at the first-principles level, we can gain valuable insight into this unusual phenomenon. A great deal of research indicates that for light ions, such as the $He^+$ ion and $\alpha$ particles ($He^{2+}$ ion), the proportionality of $S_e$ is greater at slow velocities for most targets [25–28]. The $\alpha$ decay in nuclear materials and nuclear waste can produce a high-energy $\alpha$ ion, and $\alpha$-ion-beam irradiation is often used in material modification. Therefore, the damage effect of $\alpha$-ion irradiation in materials is a very important topic for the application of nuclear materials [29] and the solidification of nuclear waste [30]. In addition, the irradiation damage and energy deposition of $\alpha$ ions in materials are still a technical problem in the application of nuclear materials [31,32]. Moreover, we chose Al films for several reasons: (1) The valence electrons of Al are the paradigm of a free-electron-like band. (2) There are some precise experimental data on the collision research for Al [33–36].

In the present work, we develop a model to simulate the collision process of projectile particles in a crystal-film target, where we combine TDDFT for electrons with molecular dynamics (MD) for ions in order to obtain unbiased microscopic insight into the ion-film interaction on the same footing in real time by considering a phase factor to avoid nontraveling states in the incident projectiles. We conduct a comparative study of $S_e$ for He ions in Al crystal films, considering the effects of the ion charge, film thickness, and temperature of the target on $S_e$.

The rest of this paper is organized as follows. First, we describe the theoretical framework, including finite-temperature models and simulation details. Second, the calculated results and discussion are presented. Finally, we summarize the conclusions of this paper.

## II. COMPUTATIONAL METHODS

In this section, the theoretical methods used in the calculation are briefly summarized. All our numerical calculations were performed using the OCTOPUS code [37] based on the real-time and real-space formulation of TDDFT. The collision system is composed of projectiles and targets. We need to prepare the projectile and target subsystems and then couple the subsystems together for the TDDFT-MD simulation. From the point of view of dynamic simulation methods, the projectile and target system is composed of ionic cores and valence electrons. Various time-dependent quantum-mechanical simulations can be successfully realized through TDDFT. In order to describe the electronic excitation produced by the projectile during the collision, the TDDFT is adopted to provide a complete dynamic description in this work. The time-dependent Kohn-Sham equations are solved in a direct manner on grids in real time and real space to describe the time evolution of the interacting electronic system [38,39] (atomic units are used unless explicitly stated),

$$i\hbar\frac{\partial}{\partial t}\psi_j(\vec{r},t)=\hat{H}\psi_j(\vec{r},t), \tag{1}$$

where $\vec{r}$ is the spatial coordinate, $t$ is time, and $\hat{H}$ is the Hamilton defined by

$$\hat{H}=-\frac{\hbar^2}{2m}\nabla^2+V_{\rm XC}(\vec{r})+V_{\rm ext}(\vec{r},t)+\int d^3\vec{r}'\frac{\rho(\vec{r}',t)}{|\vec{r}'-\vec{r}|}. \tag{2}$$

In Eq. (2), $m$ is the mass of an electron, and $V_{\rm XC}(\vec{r})$ is the exchange-correlation potential, for which we use the adiabatic generalized gradient approximation based on the Perdew-Burke-Ernzerhof functional [40]. We employed norm-conserving pseudopotentials of the Troullier-Martins form representing the ionic cores [$He^{2+}$ and Al ($1s^22s^22p^6$)] of each atomic component of the system considered [41]. $\rho(\vec{r},t)=\Sigma_j|\psi_j|^2$ is the valence-electron number density, with the index $j$ running over the occupied one-electron orbitals $\psi_j$. $V_{\rm ext}(\vec{r},t)$ is the external potential, which is formed by the ionic cores and the time-dependent field produced by the moving projectile. Newton's equation of nuclear motion follows [42,43]

$$M_k\frac{d^2\vec{R}_k}{dt^2}=F_k(t), \tag{3}$$

where $M_k$ denotes the mass of the $k$th nuclei and $\vec{R}_k$ denotes the coordinates of the $k$th ion. $F_k(t)$ is the force on the $i$th ionic core calculated from the density-functional-theory (DFT) total energy,

$$F_k(t)=-\nabla_{R_k}E[\{\vec{R}_k\},\psi_j(\vec{r},t)]. \tag{4}$$

When we model bare-ion collisions, the classical point particles are simply given an initial velocity $\vec{v}$. However, if the projectiles have bound electrons, the preparation of the initial state must be considered carefully to avoid an unphysical initial decoupling of the projectile's nucleus and electrons. Initially, both the $He^+$ ion and Al films stay in their electronic ground states, and a phase factor $e^{i\vec{v}\cdot\vec{r}}$ is added in front of each Kohn-Sham orbital (KSO) of the $He^+$ ion to boost its electronic density moving with the velocity $\vec{v}$, i.e., to boost the KSOs of the projectile system with the constant velocity $\vec{v}$: $\psi_j(\vec{r},t)\longrightarrow e^{i\vec{v}\cdot\vec{r}}\psi_j(\vec{r},t)$ [44]. The phase factor, commonly known as the electron translation factor [45,46], causes the KSOs of the $He^+$ ion to carry an additional linear momentum as well as kinematic energy.

In order to consider the temperature effect, the thermalized electronic state of Al film in the collision is described by the finite-temperature DFT. The finite-temperature DFT has been widely discussed and applied [47–51]. The implementation of the finite-temperature DFT will handle the occupation in the

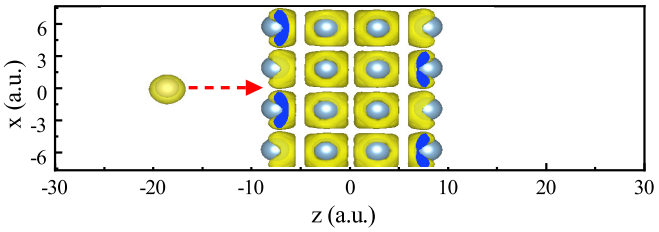


FIG. 1. Illustration of our simulation cell: a $He^+$ with a velocity of 0.3 a.u. impacts a four-layer-thick Al sheet, where one layer corresponds to about 5 a.u. The Al crystal shown is a cubic supercell with a lattice parameter of 20 a.u.; the rest are in a vacuum environment. $He^+$ is moving in the direction indicated by the red arrow. The projection positions of target aluminum atoms and projectile helium ions are overlaid with electron density.

static solution using a giant canonical ensemble. Assuming that the electron thermalization time is very short, the positions of atoms in the ground state remain in their equilibrium positions. The Kohn-Sham equation is formally written as

$$\left\{ -\frac{\hbar^2}{2m}\nabla^2 + V_{\rm XC}(\vec{r}) + V_{\rm ext}(\vec{r},t) + \int d\vec{r}'\frac{e^2}{|\vec{r}'-\vec{r}|}\rho^T(\vec{r}') \right\}\psi_j(\vec{r}) = E_j\psi_j(\vec{r}). \quad (5)$$

The electron density $\rho^T(\vec{r})$ at temperature $T$ is written as

$$\rho^T(\vec{r}) = \Sigma_j n_j^T |\psi_j(\vec{r})|^2, \quad (6)$$

where $n_j^T$ is the occupation number of the Fermi-Dirac distribution related to temperature,

$$n_j^T = \frac{1}{1+e^{(E_j-\mu)/k_BT}}, \quad (7)$$

where $E_j$ is the energy of the electron orbitals, $\mu$ is the chemical potential, and $k_BT$ is the temperature in energy units. It is worth noting that all quantities related to $\psi_j$, $E_j$, and $\mu$ depend on the temperature $T$ due to self-consistent requirements [52].

We take the coordinate system shown in Fig. 1. A cubic unit cell of Al crystal adopted from [53], containing four atoms with a lattice parameter of 7.63 a.u., is expanded into a supercell, placed in a $15 \times 15 \times 60$ a.u.$^3$ simulation box. Periodic boundary conditions for the simulation box are imposed in the $x$ and $y$ directions to describe the thin film. Different sheet thicknesses consisting of four to six Al atomic layers were studied, where one layer corresponds to about 5 a.u. The $He^+$ ion starts at a distance of at least 15 a.u. from the Al sheet and traverses it along the channeling trajectory (see Fig. 1) [54]. We selected three off-channeling trajectories, denoted as off-1, off-2, and off-3, at locations away from the center of the Al crystal (as shown in the inset of Fig. 3 below). $S_e$ of $He^+$ moving along the off-channeling trajectories is calculated and compared with the experimental value. The orbital wave functions are represented by three-dimensional spatial grid points with a mesh spacing of 0.3 a.u. corresponding to a cutoff energy of 110 Ry in the plane-wave expansion. A $2 \times 2 \times 1$ grid of Monkhorst-Pack $k$ points is used to sample the Brillouin zone. The Brillouin zone of the supercell was sampled at $(0.25, 0.25, 0)$, $(-0.25, 0.25, 0)$, $(0.25, -0.25, 0)$, and $(-0.25, -0.25, 0)$. The enforced time-reversal-symmetry integrator [55,56] with a time step of 0.01 a.u. was used to propagate the Kohn-Sham orbitals. Our simulation calculation of the collision process mainly consists of the following three steps: (1) The initial electronic states of the Al films and the ground-state single-particle orbitals of the projectile particle at a given temperature are simulated by static DFT. (2) For neutral He and the $He^+$ ion, a phase factor $e^{i\vec{v}\cdot\vec{r}}$ is artificially added in front of each KSO of the He or $He^+$ ion to boost its electronic density moving with the velocity $\vec{v}$, i.e., to boost the KSOs of the projectile system with constant velocity $\vec{v}$. (3) The ground-state wave functions of the projectile and the target are combined into a new system to perform the TDDFT simulation.

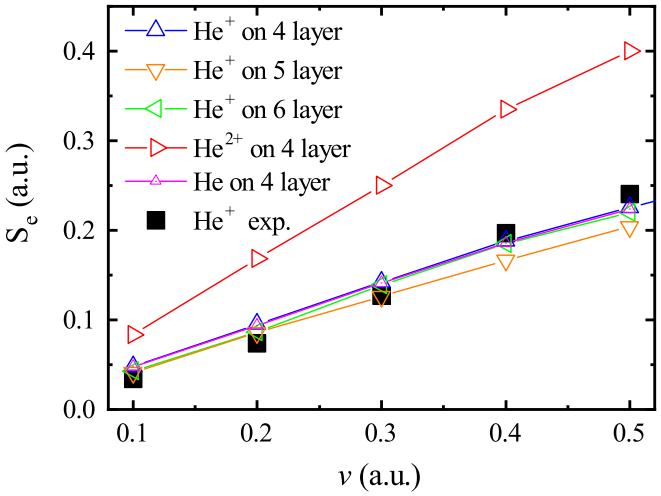


FIG. 2. Electronic stopping power of a projectile particle traversing Al films with different layers as a function of projectile velocity for the channeling trajectories. The black squares represent the experimental data [24].

## III. RESULTS AND DISCUSSION

$S_e$ can be represented by $dE/dx \approx \Delta E/\Delta x$, where $\Delta E$ is the kinetic-energy difference of the He ions. Figure 2 shows $S_e$ of the projectile particle moving through Al films with different layers, together with experimental data [24]. As far as we are aware, no direct experimental data are available for the stopping power of Al for $He^{2+}$ ions, which makes the prediction of our simulations even more important. In the low-velocity regime, i.e., $v < 0.35$ a.u., the calculated results are in good agreement with the experimental data [24]. However, with the increase of projectile velocity, the calculated results tend to be lower than the experimental data, which is an expected result. In a crystal, electrons are arranged in a shell around the nucleus of each atom. The electron density is lowest at the midpoint between two adjacent atoms. When the particle is incident along the channeling trajectories, the particle interacts primarily with valence electrons, passing through the region with the lowest average electron density in the crystal; thus, it loses the least energy [57]. Meanwhile, we calculate $S_e$ of neutral He projectiles in Al. Because He

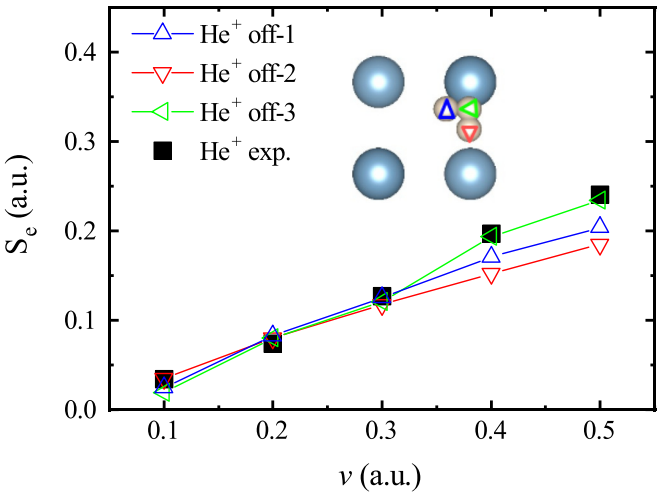


FIG. 3. Electronic stopping power of a $He^+$ ion traversing Al films with four layers as a function of projectile velocity for the off-channeling trajectories. The inset shows the top view of the incidence geometries of off-channeling trajectories. The large blue balls indicate Al atoms, the small white balls present $He^+$ ions, and the blue, red, and green triangles show the incident positions.

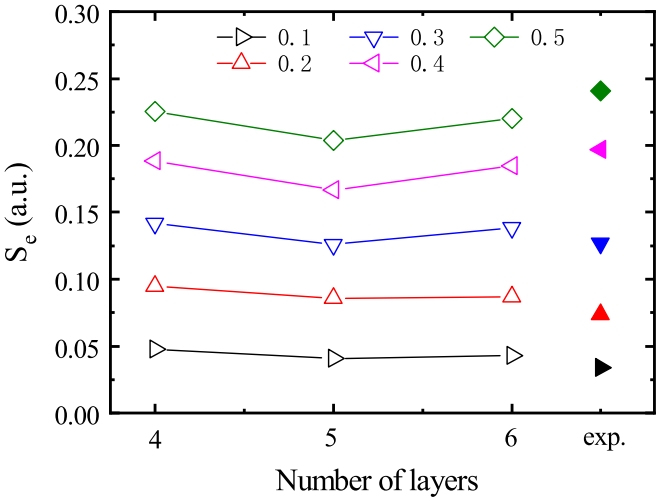


FIG. 4. Electronic stopping power of $He^+$ channeling in Al films with different thicknesses at velocities of 0.1, 0.2, 0.3, 0.4, and 0.5 a.u.. Solid symbols represent experimental stopping power at the corresponding velocities.

has bound electrons, the preparation of the initial state must be considered carefully. A phase factor $e^{i\vec{v}\cdot\vec{r}}$ is added in front of each KSO of the He to boost its electronic density moving with the velocity $\vec{v}$.

As you can see from the experimental data, $S_e$ showed deviations from the velocity proportionality for $v > 0.2$ a.u. Therefore, we calculated the stopping power of the four-layer Al film for the $He^+$ ion moving along the off-channeling trajectories and compared it with the measured data; the results are shown in Fig. 3. The inset shows the top view of the incidence points for the off-channeling geometry. We found that good agreement between our simulations and the experimental data is achieved at $v \leqslant 0.3$ a.u., and $S_e$ obtained from channel off-3 showed a significant departure from the proportionality at $v = 0.3$ a.u.

This complex velocity dependence can be ascribed to an additional energy dissipation channel. Auger electron spectroscopy showed that the formation of a molecular orbital leads to excitation of inner shells for He ions [58]. We qualitatively conclude that this additional energy dissipation channel is a repeated charge exchange between He ions and Al caused by electron excitation, indicating the presence of energy transfer [24]. Under the condition of channeling, the distance between the projectile and the target atom is slightly longer, and the excitation of the electron-hole pair is the main energy dissipation channel. However, for the off-channeling conditions, charge transfer is the important energy-loss channel. Since the energy-loss process of projectile ions is dominated by electron excitation and ionization of the system, the captured electrons must be considered in the collision process. The description of charge exchange is required for a deeper understanding of the microcosmic mechanism for $S_e$ of ions. We studied the electron transfer behavior between the ion and target atoms and calculated the number of electrons captured by the moving projectiles in real time. This is explained later in Figs. 5 and 6. Meanwhile, these results show that the TDDFT simulations can accurately reproduce $S_e$ in real systems.

To further clarify the influence of film thickness on $S_e$ and the correctness of the model employed in this work, we studied $S_e$ of $He^+$ channeling through Al films with various thicknesses and compared it with the experimental data; the results are shown in Fig. 4. The thickness of the Al film used in this work is much smaller than that in the experiment. However, by comparison, we find that $S_e$ is very close to the experimental data at different velocities, which further confirms that the thickness of the film has little effect on $S_e$.

To compare the electron-capture ability of $He^+$ and $He^{2+}$ more intuitively, we calculated the number of electrons captured by $He^+$ and $He^{2+}$ after they penetrated through the Al films. The charge surface density distribution is the sum of the electron densities of slices at different locations at different times,

$$\tilde{\rho}(z,t) = \int_{x_{\min}}^{x_{\max}} dx \int_{y_{\min}}^{y_{\max}} dy \rho(x,y,z,t), \tag{8}$$

where $x_{\min}$ ($y_{\min}$) and $x_{\max}$ ($y_{\max}$) are the upper and lower boundaries of the simulation box along the $x$ ($y$) direction, respectively. The charge-density difference distribution

$$\Delta\tilde{\rho}(z,t) = \tilde{\rho}(z,t) - \tilde{\rho}(z,t_0) \tag{9}$$

is the difference between the charge densities at different times and the initial time. The total number of electrons at a position on the $z$ axis is defined by

$$Q(z,\Delta z) = \int_{z-\Delta z}^{z+\Delta z} dz' \tilde{\rho}(z'). \tag{10}$$

Meanwhile, we also compared the influence of Al film thickness on the change in the number of electrons, i.e., $\Delta Q = Q(z_f, \Delta z_f) - Q_i$, where $Q_i$ is the charge number of the projectile particle before the collision and $z_f$ is the position of the projectile particle after collision, as shown in Fig. 5. In

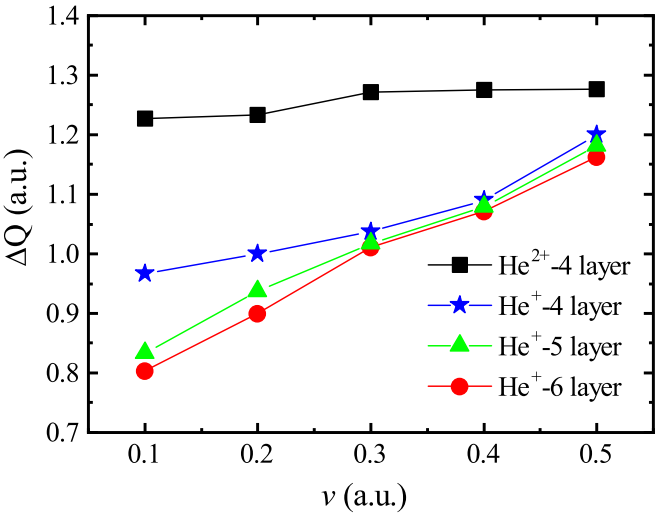


FIG. 5. The number of electrons captured by $He^+$ in Al films with different numbers of layers and $He^{2+}$ at a velocity of 0.1–0.5 a.u. The black squares denote the number of electrons captured by the $He^{2+}$ ion passing through the four-layer Al film. The blue stars represent the number of electrons captured by $He^+$ passing through the four-layer film.

this case, $\Delta z_f$ is 3 a.u. It is clear from Fig. 5 that the electron-trapping ability of the $He^{2+}$ ion is stronger than that of the $He^+$ ion. Interestingly, the number of electrons captured by the $He^+$ ion decreases for velocities between 0.1 and 0.3 a.u. as the film thickness increases. With the increase of velocity, the ability of the $He^+$ ion to capture electrons tends to be consistent for Al films with different thicknesses.

Figure 6 presents the charge-density difference distribution of $He^+$ ions traveling through an Al film at different moments obtained from Eq. (9). The range of $z$ is from $-10$ to 10 a.u., which means Al thin film. As time goes by, $He^+$ gradually moves towards the Al film until it passes through the Al film. The position where the charge density increases at every

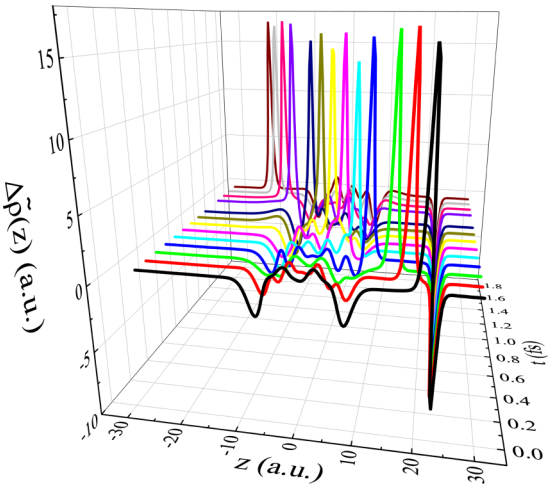


FIG. 6. The charge-density difference of induced charge when the projectile particle is moving through the Al thin film. The charge-density difference distribution $\Delta\tilde{\rho}$ is the difference between the charge-density distributions at different times and the initial time.

moment is the position of the projectile. As can be seen from Fig. 6, the projectile moves from $z = 20$ a.u. to $z = -20$ a.u. It causes charge disturbances in the film when the $He^+$ ion enters the film, resulting in charge-density changes. The oscillations reflect the periodicity of the lattice. After the ion passes through the Al film, it reaches an equilibrium charge state [59].

It can be seen from Ref. [60] that electrons can be captured by the moving ion in the process of He crossing the Al film; that is, charge exchange occurs in this process. In order to explain the charge-exchange process intuitively, we show the dynamic change process of the charge density of neutral He, a $He^+$ ion, and a $He^{2+}$ ion passing through an Al film. Figure 7 shows the distribution of the electron density of He passing through the Al film. For neutral He, it can be seen from the fluctuation of the density distribution that He loses and captures electrons in this process and a charge-changing event occurs. Similarly, there is a charge exchange for the case of $He^+$ moving in Al. In the case of $He^{2+}$, the bare ion enters the Al film, and a charge-capture process mainly takes place. It can be seen from the comparison of the initial and final charge densities in the whole process that electrons are captured by the bound state of the moving $He^{2+}$ ion. The capture of electrons by the moving ion as He particles move in the Al film can be attributed to the following mechanisms: (1) Target electrons can be transitioned from Al atoms to a bound state of the projectile particle. (2) The particle moving in the lattice is resonated by a potential field, which causes the electron to transition to the bound state of the particle. (3) The generation of electron-hole pairs and plasmons contributes to the direct capture of electrons in the conduction band.

From the point of view of the electronic structure, the difference of occupation distribution function (DOO) [52] is further analyzed at different speeds of $He^+$. Figure 8 shows the difference in DOO in Al at the beginning and end of the collision at different speeds of $He^+$. As can be seen, with increasing velocity, the position of the valley below the Fermi level moves to the left, indicating that with the increase of velocity, deep-level electrons are more likely to be excited. Moreover, by comparing DOOs above the Fermi level at different velocities, it can be found that the higher the velocities are, the easier it is for the electrons in the target system to transition to a higher energy level. From the photons' point of view, when projectile particles pass through the Al film, a changing electric field will be generated which will contain virtual photons, thus generating the DOO spectrum. We assume that a projectile with charge $q$ and velocity $v$ passes through the target from a point $(0, b, z_0)$ with impact parameter $b$, as shown in Fig. 9(a). Electric and magnetic fields in the $y$ and $z$ directions will be generated at the zero point of the coordinates. The magnetic-field effect is ignored, and the equivalent electric field can be obtained from the following equation:

$$E_y(t) = q\frac{\gamma b}{(b^2+\gamma^2 v^2 t^2)^{3/2}},$$
$$E_z(t) = -q\frac{\gamma vt}{(b^2+\gamma^2 v^2 t^2)^{3/2}}, \quad (11)$$

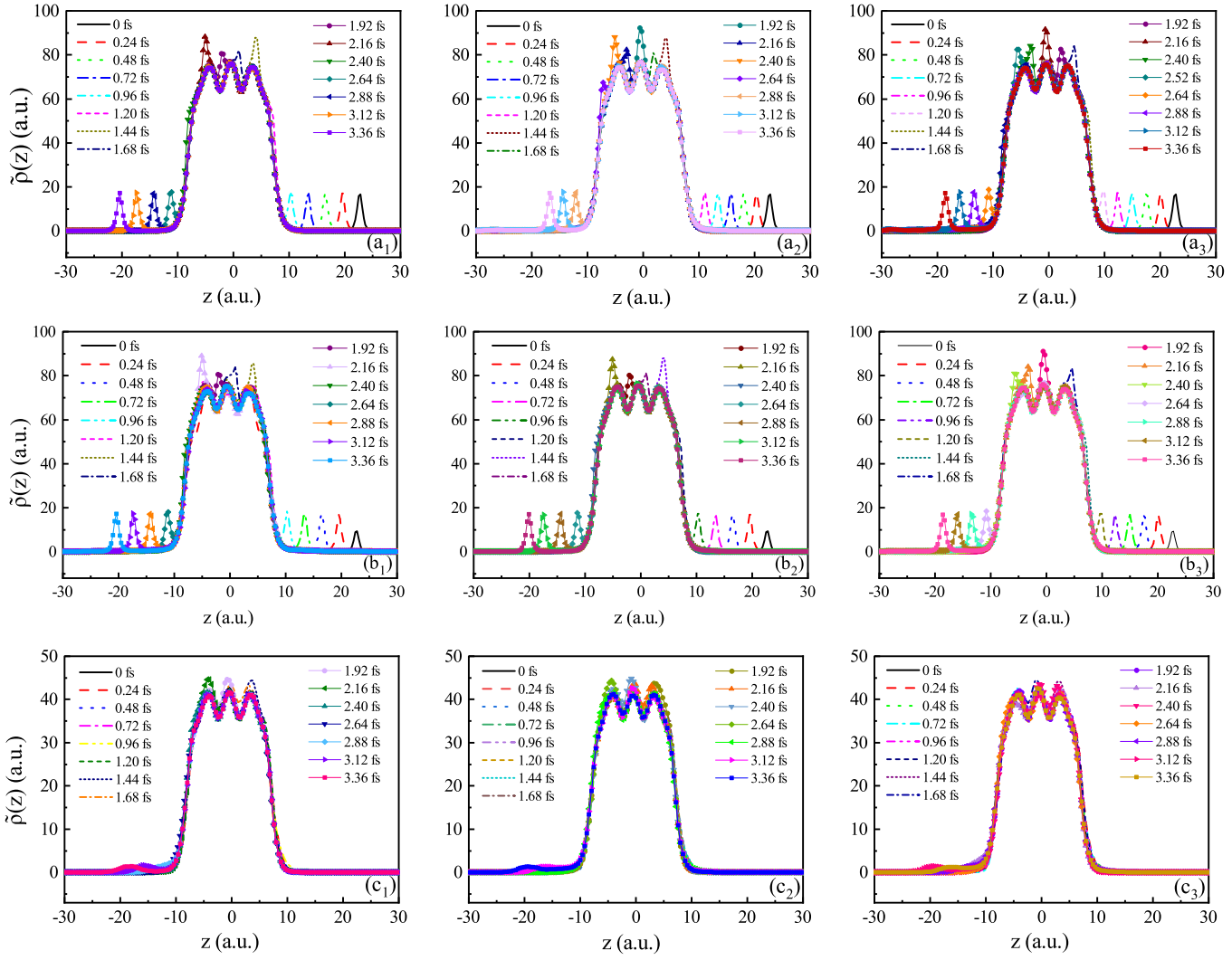


FIG. 7. The distribution of electron density of He passing through the Al film. (a1)–(a3) The charge-density distribution of the neutral He at $v = 0.1$, 0.3, and 0.5, respectively. (b1)–(b3) The charge-density distribution of $He^+$ at $v = 0.1$, 0.3, and 0.5, respectively. (c1)–(c3) The charge-density distribution of $He^{2+}$ at $v = 0.1$, 0.3, and 0.5, respectively. The abscissa indicates that along the crystal direction, the distance from $-10$ to 10 a.u. is the Al film, and the remainder is the vacuum environment. The incident process is from $z = 20$ a.u. to $z = -20$ a.u.

with the relations $\beta = v/c$ and $\gamma = (1 - \beta^2)^{-1/2}$, where $c$ is the speed of light in vacuum.

Figures 9(b) and 9(c) show the electric field in the $y$ and $z$ directions at different incident velocities, respectively. $E_y(\omega)$ and $E_z(\omega)$ are the Fourier transforms of $E_y(t)$ and $E_z(t)$, as shown in Figs. 9(d) and 9(e). Consistent with the above conclusions, higher-velocity projectiles contain more high-frequency photons, so they are more likely to excite deep-level electrons, and target electrons are more likely to be excited to higher energy levels.

Bransden *et al.* [61] emphasized that electron transfer factors should be used in collision theory. Therefore, we are curious about the influence of phase factors in $S_e$. In this work, we add a phase factor $e^{i\vec{v}\cdot\vec{r}}$ in front of each KSO of the $He^+$ ion to boost its electronic density moving with the velocity $\vec{v}$, i.e., to boost the KSOs of the projectile system with the constant velocity $\vec{v}$. Figure 10 shows a comparison of the results of the calculation model with and without phase factors $e^{i\vec{v}\cdot\vec{r}}$. We found that at low velocities, such as 0.1–0.7 a.u., the phase factor has nearly no effect on $S_e$, but the effect of the phase factor begins to emerge as the projectile velocity continues to increase. From the theoretical point of view, the influence of the phase factor may be greater when calculating higher-velocity projectiles. Therefore, we should consider the influence of the phase factor when calculating $S_e$ for fast projectiles. At the same time, considering the phase factor, the change in slope around $v = 1.2$ a.u. may be due to the active charge transfer behavior of the channeling ion.

To the best of our knowledge, temperature should remain one of the most important variables acting on the stopping power of the material and participating in the mechanisms of electronic stopping and nuclear stopping. This is relevant because temperature can modify the stopping power of the material, which is actually a consequence of the change in the respective electronic and nuclear structures. Despite its fundamental role, this variable is ignored in most theoretical approaches utilized to characterize the $S_e$ attributes of materials. Particularly, the TDDFT model assumes that the

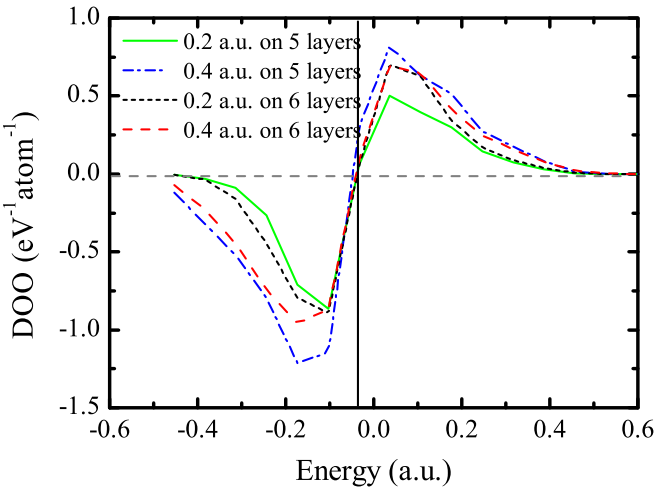


FIG. 8. The difference in the occupation distribution function in Al at the beginning and end of the collision at different speeds of $He^+$. The vertical black solid line indicates the Fermi level $E_F$, and the gray dashed line represents the zero line.

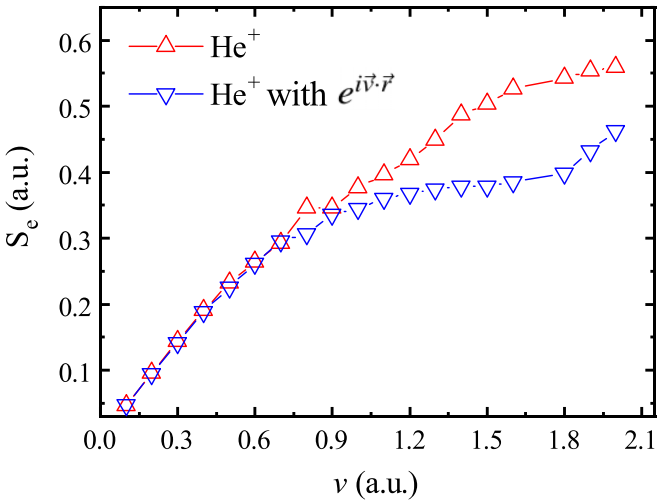


FIG. 10. Comparison of the stopping power of the $He^+$ ion obtained from different model methods for the center channeling trajectories.

initial temperature of the target material is zero, so that the $S_e$ properties at finite temperature remain neglected under this approach. Therefore, we are curious whether temperature in the target atoms influences $S_e$ of the projectile at a given temperature. The temperature effect of the target atoms can be divided into two categories, including the temperature effect of the target electrons and the temperature effect of the target ions. Furthermore, the temperature effect of the target ions can be considered from two aspects, namely, displacement and energy dissipation of the target ions. Next, we consider the temperature effect of the target electrons. The calculated $S_e$ at target electron temperatures of 100, 300, and 500 K are shown in Fig. 11. The results show that the target electron's temperature has little effect on $S_e$. We have shown that the temperature effect of the target electrons is not significant over the temperature range considered. We further study how the displacement effect of the target ions affects $S_e$.

To directly confirm the expansion effect of the target ions, MD simulations of up to 10 ps at 300 and 500 K were performed on the target system. Five samples were uniformly selected from the results of the MD simulation to calculate $S_e$. Then $S_e$ calculated from five samples were averaged, and the results are shown in Fig. 12. The orange triangles and line in Fig. 12 represent $S_e$ without considering the temperature

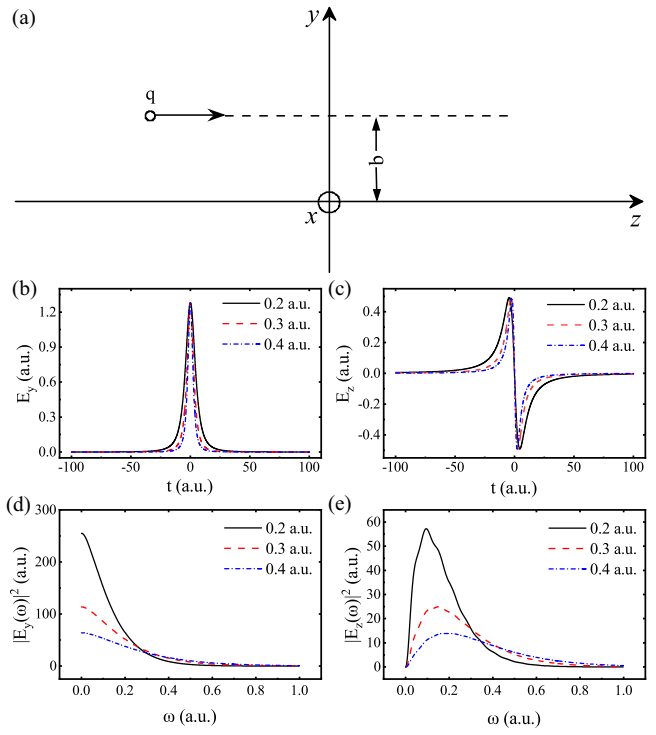


FIG. 9. (a) Schematic illustration of incident charged particles. (b) and (c) The electric field along the $y$ and $z$ directions excited by charged particles, respectively. (d) and (e) Spectrum diagrams of the corresponding electric field.

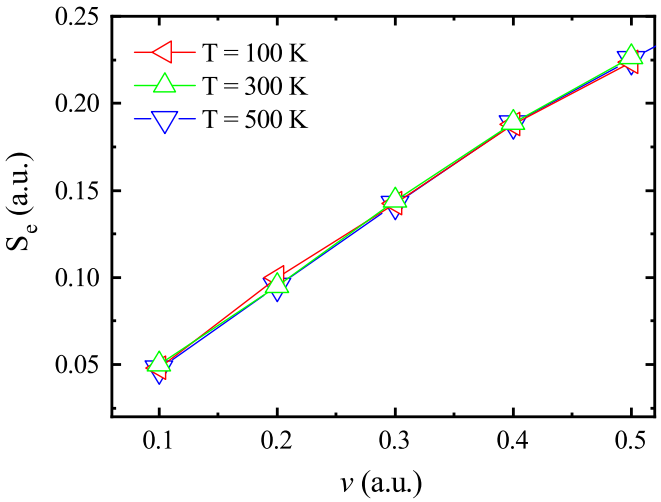


FIG. 11. Considering the finite electron temperature, $S_e$ of the $He^+$ ion traversing Al films as a function of projectile velocity.

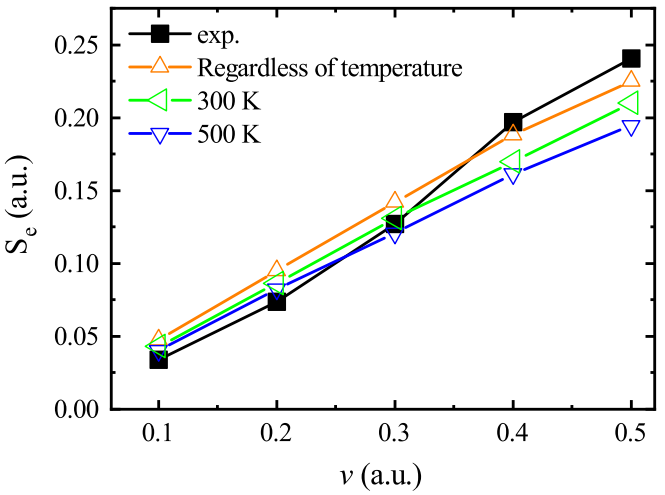


FIG. 12. Considering the displacement of target ions, $S_e$ of the $He^+$ ion traversing Al films as a function of projectile velocity at finite target-ion temperature.

effect of the target atoms. Our frozen-target model further elucidates the displacement effect of the target ions. Heating causes lattice expansion, so when incident ions pass through a target material with lower electron density, $S_e$ decreases.

For a more intuitive understanding of the expansion effect of the target ions, we count atomic pairs found at distance $r$ using the pair distribution function (PDF). In practice, we take each atom as the origin of coordinates, the number of atoms $N$ within the spherical shell $r \sim r + \Delta r$ is counted, and an average number of atoms $\langle N \rangle$ at distance $r$ is then obtained. A probability distribution can be defined as

$$G(r) = \frac{\langle N \rangle}{4\pi r^2 \Delta r}. \tag{12}$$

Figure 13 shows the PDF for the structure of Al films at ionic temperatures of 300 and 500 K. It can be seen from Fig. 13 that the structure of the Al film is basically stable at a given ion temperature after a MD simulation of 10 ps. The displacement of the target ion can result in two trends that change $S_e$. The target ion is closer to the center of the lattice channel after displacement, which leads to an increase of $S_e$. The target ion is farther away from the center of the lattice channel after displacement, which leads to a decrease of $S_e$. As the temperature increases, the target ions are more likely to appear farther away from the lattice channel than closer to the center of the lattice channel, so the average displacement of the target ions will lead to a decreasing trend of $S_e$ with the increase of temperature.

Finally, we study how the energy dissipation of target ions affects $S_e$. The orange triangles and line in Fig. 14 represent $S_e$ without considering the temperature effect of the target atoms, the green and blue lines show $S_e$ of a $He^+$ ion traversing Al films as a function of projectile velocity at ionic temperatures of 300 and 500 K, respectively. When studying the energy dissipation of target ions, in order to prevent the influence of the surface effect of the thin film, we fixed four layers of atoms on the surface, and the remaining atoms were not fixed. For a given ion density within a material, the energy dissipation of target ions increases with increasing temperature, resulting

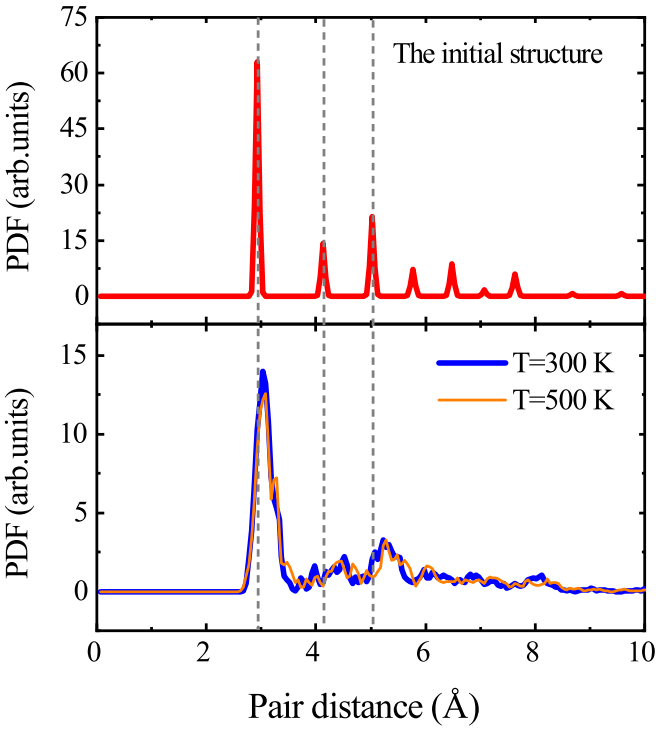


FIG. 13. Pair distribution functions for the structure of Al films at ion temperatures of 300 and 500 K. Top: Pair distribution functions for initial structure. Bottom: Pair distribution function of the structure after 10 ps MD.

in an increase in $S_e$ with increasing temperature. In conclusion, the influence of the target ion's temperature on $S_e$ can be considered from two aspects. The displacement of target ions decreases $S_e$ with increasing temperature. In addition, the energy dissipation of target ions causes $S_e$ to increase with the increase in temperature.

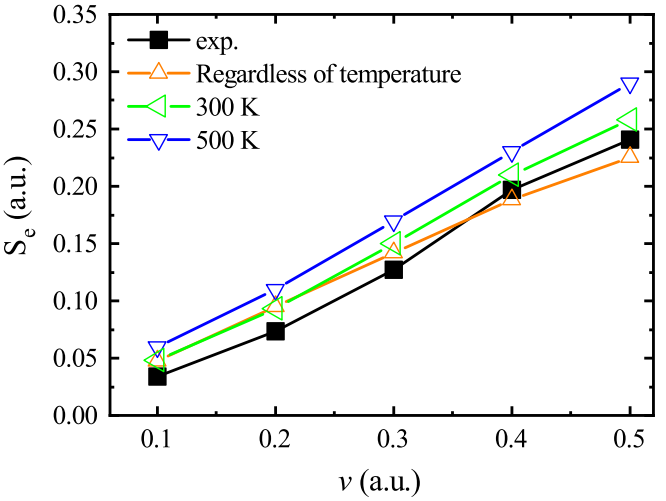


FIG. 14. Considering the energy dissipation of target ions, $S_e$ of the $He^+$ ion traversing Al films as a function of projectile velocity at finite target-ion temperature.

## IV. SUMMARY

When a particle moves through a solid material, it is angularly dispersed and loses its kinetic energy to both the ions and the electrons inside the material. Apparently, although experiments generally access only spatially and time-averaged quantities, simulating the dynamics of electrons and ions in real-time simulations at the first-principles level not only in real time but also in real space could help us to have a thorough and detailed understanding of the microcosmic mechanism of $S_e$. In this paper, we have developed a model to simulate the collision process of projectile particles in a crystal-film target, where we combined TDDFT for electrons with MD for ions in order to obtain unbiased microscopic insight into the ion-film interaction on the same footing in real time by considering a phase factor to avoid nontraveling states in the incident projectiles. We conducted a comparative study of $S_e$ for He ions in Al crystal films, considering the effects of the ion charge, film thickness, and temperature of target on $S_e$. Our calculated stopping powers are in good agreement with the experimental data and reproduced the deviation from velocity proportionality found in the experimental results for a $He^+$ ion in Al, validating our approach and numerical implementation.

Interesting enough, the effect of the target temperature on target stopping power can be divided into two aspects which are derived from the target electron and target ion. Below 500 K, the effect of the target-electron temperature on target stopping power is almost negligible. The influence of the target-ion temperature on target stopping power can be divided into two aspects which are derived from the displacement and energy dissipation of target ions. The displacement of the target ion can result in two trends that change the target stopping power: (1) The target ion is closer to the center of the lattice channel after displacement, which leads to the increase in target stopping power. (2) The target ion is farther away from the center of lattice channel after displacement, which leads to the decrease in target stopping power. As the temperature increases, the target ions are more likely to appear farther away from the lattice channel than closer to the center of the lattice channel, so the average displacement of the target ions will lead to a decreasing trend of the target stopping power with the increase in temperature. Under the condition of a given ionic density in the target, the energy dissipation capacity of target ions increases with the increase in temperature, resulting in the tendency of the target stopping power to increase with increasing temperature. Generally, the stopping powers of materials, dictated by their electronic and crystallographic structures, are largely set at the synthesis and fabrication stages. Further *in situ* tuning may be achieved by changing the temperature and pressure. $S_e$ of various materials at finite temperature deserve to be investigated in future research both theoretically and experimentally.

## ACKNOWLEDGMENTS

This work was supported by the National Natural Science Foundation of China (Grants No. 51735001, No. 11975119, and No. 11774030) and the Beijing Natural Science Foundation (Grant No. 2192049).

[1] G. H. Rinehart, Prog. Nucl. Energy **39**, 305 (2001).
[2] L. J. Deutsch, C. Salvo, and D. Woerner, Acta Astronaut. **46**, 229 (2000).
[3] X. Wang and J. R. Key, Science **299**, 1725 (2003).
[4] F. Shi, P. Ramesh, and S. Mukherjee, Comput. Struct. **56**, 769 (1995).
[5] L. Walters, D. Porter, and D. Crawford, Prog. Nucl. Energy **40**, 513 (2002).
[6] C. K. Li, F. Mao, Y. L. Fu, B. Liao, X. P. Ouyang, and F. S. Zhang, Nucl. Instrum. Methods Phys. Res., Sect. B **392**, 51 (2017).
[7] S. Thomson, Philos. Mag. **23**, 449 (1912).
[8] M. Hentschel, R. Kienberger, C. Spielmann, G. A. Reider, N. Milosevic, T. Brabec, P. Corkum, U. Heinzmann, M. Drescher, and F. Krausz, Nature (London) **414**, 509 (2001).
[9] G. Sansone, E. Benedetti, F. Calegari, C. Vozzi, L. Avaldi, R. Flammini, L. Poletto, P. Villoresi, C. Altucci, R. Velotta, S. Stagira, S. De Silvestri, and M. Nisoli, Science **314**, 443 (2006).
[10] E. Goulielmakis, M. Schultze, M. Hofstetter, V. S. Yakovlev, J. Gagnon, M. Uiberacker, A. L. Aquila, E. M. Gullikson, D. T. Attwood, R. Kienberger, F. Krausz, and U. Kleineberg, Science **320**, 1614 (2008).
[11] M. J. Abel, T. Pfeifer, P. M. Nagel, W. Boutu, M. J. Bell, C. P. Steiner, D. M. Neumark, and S. R. Leone, Chem. Phys. **366**, 9 (2009).
[12] F. Ferrari, F. Calegari, M. Lucchini, C. Vozzi, S. Stagira, G. Sansone, and M. Nisoli, Nat. Photonics **4**, 875 (2010).
[13] K. Zhao, Q. Zhang, M. Chini, Y. Wu, X. Wang, and Z. Chang, Opt. Lett. **37**, 3891 (2012).
[14] F. Frank, C. Arrell, T. Witting, W. A. Okell, J. McKenna, J. S. Robinson, C. A. Haworth, D. Austin, H. Teng, I. A. Walmsley, J. P. Marangos, and J. W. G. Tisch, Rev. Sci. Instrum. **83**, 071101 (2012).
[15] E. J. Takahashi, P. Lan, O. D. Mücke, Y. Nabekawa, and K. Midorikawa, Nat. Commun. **4**, 2691 (2013).
[16] T. Hammond, G. G. Brown, K. T. Kim, D. Villeneuve, and P. Corkum, Nat. Photonics **10**, 171 (2016).
[17] X. Ren, J. Li, Y. Yin, K. Zhao, A. Chew, Y. Wang, S. Hu, Y. Cheng, E. Cunningham, Y. Wu, Michael Chini and Z. Chang, J. Opt. **20**, 023001 (2018).
[18] A. V. Krasheninnikov, Y. Miyamoto, and D. Tománek, Phys. Rev. Lett. **99**, 016104 (2007).
[19] A. Ojanperä, A. V. Krasheninnikov, and M. Puska, Phys. Rev. B **89**, 035120 (2014).
[20] A. Arnau, M. Penalba, P. Echenique, and F. Flores, Nucl. Instr. Meth. Phys. Res. B **69**, 102 (1992).
[21] E. Fermi and E. Teller, Phys. Rev. **72**, 399 (1947).
[22] R. H. Ritchie, Phys. Rev. **114**, 644 (1959).
[23] P. M. Echenique, F. Flores, and R. H. Ritchie, Solid State Phys. **43**, 229 (1990).

[24] D. Primetzhofer, S. Rund, D. Roth, D. Goebl, and P. Bauer, Phys. Rev. Lett. **107**, 163201 (2011).
[25] G. Martínez-Tamayo, J. C. Eckardt, G. H. Lantschner, and N. R. Arista, Phys. Rev. A **54**, 3131 (1996).
[26] D. Goebl, D. Roth, and P. Bauer, Phys. Rev. A **87**, 062903 (2013).
[27] C.-K. Li, F. Wang, B. Liao, X.-P. OuYang, and F.-S. Zhang, Phys. Rev. B **96**, 094301 (2017).
[28] D. Roth, B. Bruckner, G. Undeutsch, V. Paneta, A. I. Mardare, C. L. McGahan, M. Dosmailov, J. I. Juaristi, M. Alducin, J. D. Pedarnig, R. F. Haglund, D. Primetzhofer, and P. Bauer, Phys. Rev. Lett. **119**, 163401 (2017).
[29] H. Matzke, Nucl. Instrum. Methods Phys. Res., Sect. B **65**, 30 (1992).
[30] A. Abbas, Y. Serruys, D. Ghaleb, J. Delaye, B. Boizot, B. Reynard, and G. Calas, Nucl. Instrum. Methods Phys. Res., Sect. B **166–167**, 445 (2000).
[31] Y. Zhang and W. J. Weber, Appl. Phys. Lett. **83**, 1665 (2003).
[32] Y. Zhang, J. Jensen, G. Possnert, D. A. Grove, I.-T. Bae, and W. J. Weber, Nucl. Instrum. Methods Phys. Res., Sect. B **261**, 1180 (2007).
[33] M. Quijada, A. G. Borisov, I. Nagy, R. Díez Muiño, and P. M. Echenique, Phys. Rev. A **75**, 042902 (2007).
[34] S. P. Møller, E. Uggerhøj, H. Bluhme, H. Knudsen, U. Mikkelsen, K. Paludan, and E. Morenzoni, Phys. Rev. A **56**, 2930 (1997).
[35] S. P. Møller, A. Csete, T. Ichioka, H. Knudsen, U. I. Uggerhøj, and H. H. Andersen, Phys. Rev. Lett. **88**, 193201 (2002).
[36] S. P. Møller, A. Csete, T. Ichioka, H. Knudsen, U. I. Uggerhøj, and H. H. Andersen, Phys. Rev. Lett. **93**, 042502 (2004).
[37] M. A. Marques, A. Castro, G. F. Bertsch, and A. Rubio, Comput. Phys. Commun. **151**, 60 (2003).
[38] V. Peuckert, J. Phys. C **11**, 4945 (1978).
[39] A. Zangwill and P. Soven, Phys. Rev. A **21**, 1561 (1980).
[40] J. P. Perdew, K. Burke, and M. Ernzerhof, Phys. Rev. Lett. **77**, 3865 (1996).
[41] N. Troullier and J. L. Martins, Phys. Rev. B **43**, 1993 (1991).
[42] Z. Wang, S.-S. Li, and L.-W. Wang, Phys. Rev. Lett. **114**, 063004 (2015).
[43] J. B. Delos and W. R. Thorson, Phys. Rev. A **6**, 720 (1972).
[44] W. Yu, C.-Z. Gao, S. A. Sato, A. Castro, A. Rubio, and B. Wei, Phys. Rev. A **103**, 032816 (2021).
[45] D. R. Bates and R. McCarroll, Proc. R. Soc. London, Ser. A **245**, 175 (1958).
[46] S. Qin, C. Gao, W. Yu, and Y. Qu, Chin. Phys. Lett. **38**, 063101 (2021).
[47] N. D. Mermin, Phys. Rev. **137**, A1441 (1965).
[48] S. Pittalis, C. R. Proetto, A. Floris, A. Sanna, C. Bersier, K. Burke, and E. K. U. Gross, Phys. Rev. Lett. **107**, 163001 (2011).
[49] K. Shiratori and K. Nobusada, J. Phys. Chem. A **112**, 10681 (2008).
[50] V. Recoules, J. Clérouin, G. Zérah, P. M. Anglade, and S. Mazevet, Phys. Rev. Lett. **96**, 055503 (2006).
[51] S. M. Vinko *et al.*, Phys. Rev. Lett. **104**, 225001 (2010).
[52] S. A. Sato, Y. Shinohara, T. Otobe, and K. Yabana, Phys. Rev. B **90**, 174303 (2014).
[53] http://aflowlib.org/search/.
[54] A. Kononov and A. Schleife, Phys. Rev. B **102**, 165401 (2020).
[55] A. Castro, M. A. L. Marques, and A. Rubio, J. Chem. Phys. **121**, 3425 (2004).
[56] E. W. Draeger, X. Andrade, J. A. Gunnels, A. Bhatele, A. Schleife, and A. A. Correa, J. Parallel Distrib. Comput. **106**, 205 (2017).
[57] W. Brandt, Sci. Am. **218**, 90 (1968).
[58] P. Riccardi, A. Sindona, and C. A. Dukes, Phys. Lett. A **381**, 1174 (2017).
[59] C.-K. Li, S. Liu, Q. Cao, F. Wang, Xiao-ping OuYang, and F.-S. Zhang, Phys. Rev. A **100**, 052707 (2019).
[60] A. Arnau, M. Pealba, P. M. Echenique, F. Flores, and R. H. Ritchie, Phys. Rev. Lett. **65**, 1024 (1990).
[61] B. H. Bransden, M. R. C. McDowell, and E. J. Mansky, Phys. Today **46**(10), 124 (1993).